

<https://doi.org/10.1038/s41699-024-00501-9>

Phonon transport manipulation in TiSe_2 via reversible charge density wave melting

Check for updates

Martí Raya-Moreno¹, Claudio Cazorla², Enric Canadell^{1,3} & Riccardo Rurali¹ ✉

Titanium diselenide (TiSe_2) is a layered material that under a critical temperature of $T_c \approx 200$ K features a periodic modulation of the electron density, known as charge density wave (CDW), which finds applications in quantum information and emerging electronic devices. Here, we present first-principles calculations showing the suppression of the CDW via photoexcitation and consequent stabilization of the undistorted high-temperature phase, in agreement with experimental observations. Interestingly, the unfolded CDW melting is accompanied by a sizable reduction in the thermal conductivity, κ , of up to 25% and a large entropy increase of $\sim 10 \text{ J K}^{-1} \text{ kg}^{-1}$. The significant κ variation is almost entirely originated from photoinduced changes in the phonon–phonon scattering processes involving a high-symmetry soft phonon mode. Our results open new possibilities in the design of devices for thermal management and phonon-based logic, and suggest original applications in the of context solid-state cooling.

The development of phononic devices^{1–3}—which instead of charge carriers use phonons, the quanta of lattice vibrations, to encode information—is subordinated to finding materials with fast, reversible, and dynamical modulation of their thermal transport properties. Active control of the thermal conductivity, κ , also plays an important role in thermal management applications⁴ (e.g., to regulate batteries' self-generated heat⁵) and thermoelectric energy harvesting⁶. Nonetheless, dynamical κ modulation poses an extraordinary practical challenge: phonons are quasi-particles that neither have mass nor bare charge, thus controlling their propagation by means of external fields is far from straightforward. In this context, both experiments^{7–10} and theory^{11–15} have pointed to a promising route based on the writing/erasing of domain walls in ferroelectrics. More generally, external electric and magnetic fields, separately^{16–22} or jointly²³, can be used to manipulate the lattice of polar/polarizable and magnetic materials, thus leading to large structural and thermal conductivity changes.

TiSe_2 is a prototypical charge density wave (CDW) material that features a periodic modulation of the electron density below a critical temperature of $T_c \approx 200$ K. Due to a coupling between the electronic and lattice degrees of freedom, the CDW originates a 2×2 commensurate lattice distortion (Fig. 2a). Interestingly, this CDW can be melted by impurity doping or light absorption^{24–28}, leading to the stabilization of the undistorted 1×1 high-temperature phase. The physical mechanism driving this phase transition consists of the creation of a threshold density of mobile charges in the valence (holes) and/or conduction (electrons) bands. Experimentally, it has been shown that photoinduced CDW melting is an ultrafast and reversible

process that occurs in the scale of picoseconds²⁶. The thermodynamic and thermal transport changes associated with such a singular photoinduced CDW $2 \times 2 \leftrightarrow 1 \times 1$ phase transition, however, remain poorly investigated to date.

The first proposals for a phononic transistor were entirely based on thermal concepts, where the heat flux between the source and drain was controlled by a thermal gate signal (i.e., the gate temperature)²⁹. Yet, as mentioned above, alternative approaches in which the heat flux is modulated by an external field appear to be much more reliable and appropriate for practical implementations (e.g., faster commutation frequencies). In particular, the possibility of manipulating κ with light emerges as a very promising avenue since, despite having received very little attention thus far, is well suited for miniaturization and could simplify the design of logic devices (i.e., no need for electrical contacts).

In this paper, we investigate with theoretical first-principles methods the changes in thermal conductivity and thermodynamic properties of a TiSe_2 monolayer (1L) upon photoinduced CDW melting at temperatures below T_c . A substantial κ reduction of up to 25% is predicted that we almost entirely ascribe to the changing anharmonic nature of a specific high-symmetry soft phonon mode driven by photoexcitation. In addition, a large light-induced phase transition entropy change is estimated which suggests the existence of sizable photocaloric effects in 1L- TiSe_2 . Notice that, although these effects should also be observed in few-layer and bulk TiSe_2 , which also feature a CDW instability³⁰, light absorption can be achieved more efficiently in single layers and thin films and thus we focus on this system.

¹Institut de Ciència de Materials de Barcelona, ICMAB-CSIC, Bellaterra, Spain. ²Departament de Física, Universitat Politècnica de Catalunya, Barcelona, Spain.³Royal Academy of Sciences and Arts of Barcelona Chemistry Section, Barcelona, Spain. ✉e-mail: rurali@icmab.es

Methods

Lattice thermal conductivity

We performed density-functional theory (DFT) calculations with the VASP code^{31,32} using the projector-augmented wave (PAW) method^{33,34} with a plane-wave cutoff of 300 eV. We have used the local density approximation (LDA) for the exchange-correlation as parameterized by Perdew and Zunger³⁵ to Ceperley and Alder data³⁶. The different unit cells used as a basis for our whole set of calculations were optimized under strict criteria of convergence by relaxing the atomic positions until all forces were lower than 10^{-7} eV/Å with the lattice parameter fixed to the experimental value^{37–39} of 3.598 Å and sampling the Brillouin zone of the CDW 2×2 (undistorted 1×1) phase with an $18 \times 18 \times 1$ ($36 \times 36 \times 1$) mesh of \mathbf{k} -points.

The harmonic interatomic force constants (IFC), needed to compute phonon frequencies, eigenvectors, and group velocities, were obtained using the supercell method as implemented in phonopy⁴⁰ using a $6 \times 6 \times 1$ and $3 \times 3 \times 1$ supercell for the undistorted 1×1 and CDW 2×2 phases, respectively. Similarly, third-order force constants, needed for the computation of three-phonon matrix elements were obtained with the method implemented in thirdorder.py⁴¹, using the same supercells with a cutoff, so that only interactions up to 0.73 nm (equivalent to 6th nearest neighbors of the 1×1 phase) were considered (convergence tests are shown in Fig. 1a).

The IFCs were then used as input to solve the phonon Boltzmann transport equation (BTE) using almaBTE, in a $50 \times 50 \times 1$ ($25 \times 25 \times 1$) Γ -centered \mathbf{q} -mesh for the 1×1 (CDW) phase (see Fig. 1b). Within the relaxation time approximation (RTA), the lattice thermal conductivity reads

$$\kappa_{\alpha\beta} = \sum_{\lambda} C_{\lambda} \frac{v_{\lambda\alpha} v_{\lambda\beta}}{|v_{\lambda}|} \Lambda_{\lambda}, \quad (1)$$

where the sum runs over all phonon modes, the index λ including both \mathbf{q} -point and phonon band; C_{λ} is the contribution of mode λ to $C(T)$, the volumetric heat capacity, v is the group velocity and Λ_{λ} is the mean free path. However, the RTA has some notorious shortcomings, which are particularly critical in two-dimensional systems, where momentum-conserving phonon–phonon processes are important. Therefore, here we adopt a full solution of the phonon BTE, beyond the RTA, that fully accounts for all scattering terms. The lattice thermal conductivity is obtained as

$$\kappa_{\alpha\beta} = \sum_{\lambda} C_{\lambda} v_{\lambda\alpha} F_{\lambda\beta}, \quad (2)$$

where F_{λ} is a generalized mean free path.

We used a broadening parameter fixed to 1 for energy conservation within a symmetric adaptive smearing approach⁴², which is a modification of the original scheme⁴¹ to properly account for microscopic reversibility

and permutation symmetry:

$$\delta(\omega_i \pm \omega_j - \omega_k) \approx \frac{1}{\sqrt{2\pi}\sigma_{ijk}} e^{-\frac{(\omega_i \pm \omega_j - \omega_k)^2}{2\sigma_{ijk}^2}} \quad (3)$$

$$\sigma_{ijk} = a\sqrt{\sigma_i^2 + \sigma_j^2 + \sigma_k^2}, \quad (4)$$

$$\sigma_i = \frac{1}{\sqrt{12}} \left\| \left\{ G_{\mu\alpha}^T \cdot N_{\mu\mu}^{-1} \right\}^T \cdot (v_i)_{\alpha} \right\|, \quad (5)$$

where i, j , and k indicate phonon states, μ indicates a reciprocal-space lattice vector, α indicates a Cartesian axis, $G_{\mu\alpha}$ is the reciprocal lattice, $N_{\mu\mu}$ is a diagonal matrix with the \mathbf{q} -grid size, a is the broadening parameter, and v is the phonon group velocity.

Light excitation is effectively accounted for through the use of the smearing parameter that controls how the partial occupancies are set for each orbital. We used a Gaussian smearing for VASP calculations, while we opted for Fermi–Dirac smearing in the electronic transport calculations described below, providing thus full consistency between the electronic temperature and smearing width, which is necessary for the computation of transport coefficients. A correspondence between the two smearing schemes has been obtained by mapping the evolution of the frequency of the soft mode at the M point (i.e., we considered two smearing widths to be equivalent if they yielded the same frequency for the soft mode). For the case of doping, harmonic IFCs used for the computation of phonon dispersions (top row of Fig. 2 in the main text) were obtained by adding a finite electron density n_e to the self-consistency cycle (and thus to the conduction band) of the structural relaxation of the unit cell; in the $6 \times 6 \times 1$ supercell calculations needed to calculate finite differences of the forces, the doping charge was appropriately rescaled like $6^2 n_e$. For the case of photoexcitation, where $n_e = 0$, harmonic and anharmonic IFCs were computed in the standard way without following any special prescription other than using the same smearing factor both in the unit cell and supercell calculations.

Electron–phonon scattering is not included in our lattice thermal conductivity calculations. Note, however, that neglecting such a source of possible phonon scattering is expected to be only relevant for the light-stabilized 1×1 undistorted phase, since this presents mobile charges in the conduction band. In fact, in a previous work by Dongre et al.⁴³ it has been explicitly shown that phonon–electron scattering in archetypal insulator materials is only pertinent at high doping concentrations. As a consequence, the change of the thermal conductivity that we estimate turns out to be a lower bound of the actual value, since electron–phonon scattering would further decrease the κ of the light-stabilized phase.

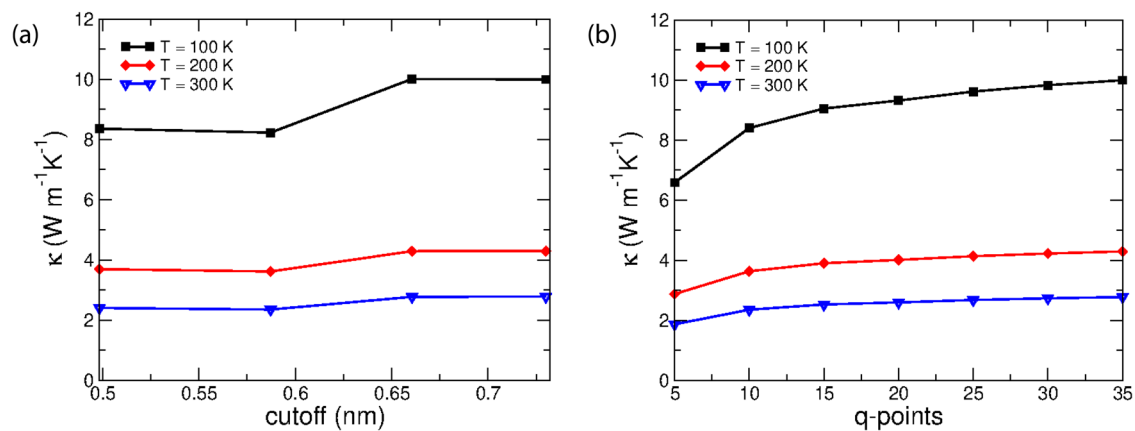


Fig. 1 | Convergence study of the thermal conductivity, κ , of the 2×2 CDW phase. **a** κ as a function of the cutoff beyond which interactions in the third-order force constants are neglected; the \mathbf{q} -point mesh is $35 \times 35 \times 1$; **b** κ as a function of different

$N \times N \times 1$ mesh of \mathbf{q} -points used to solve the BTE; the cutoff for third-order interactions is 0.73 nm.

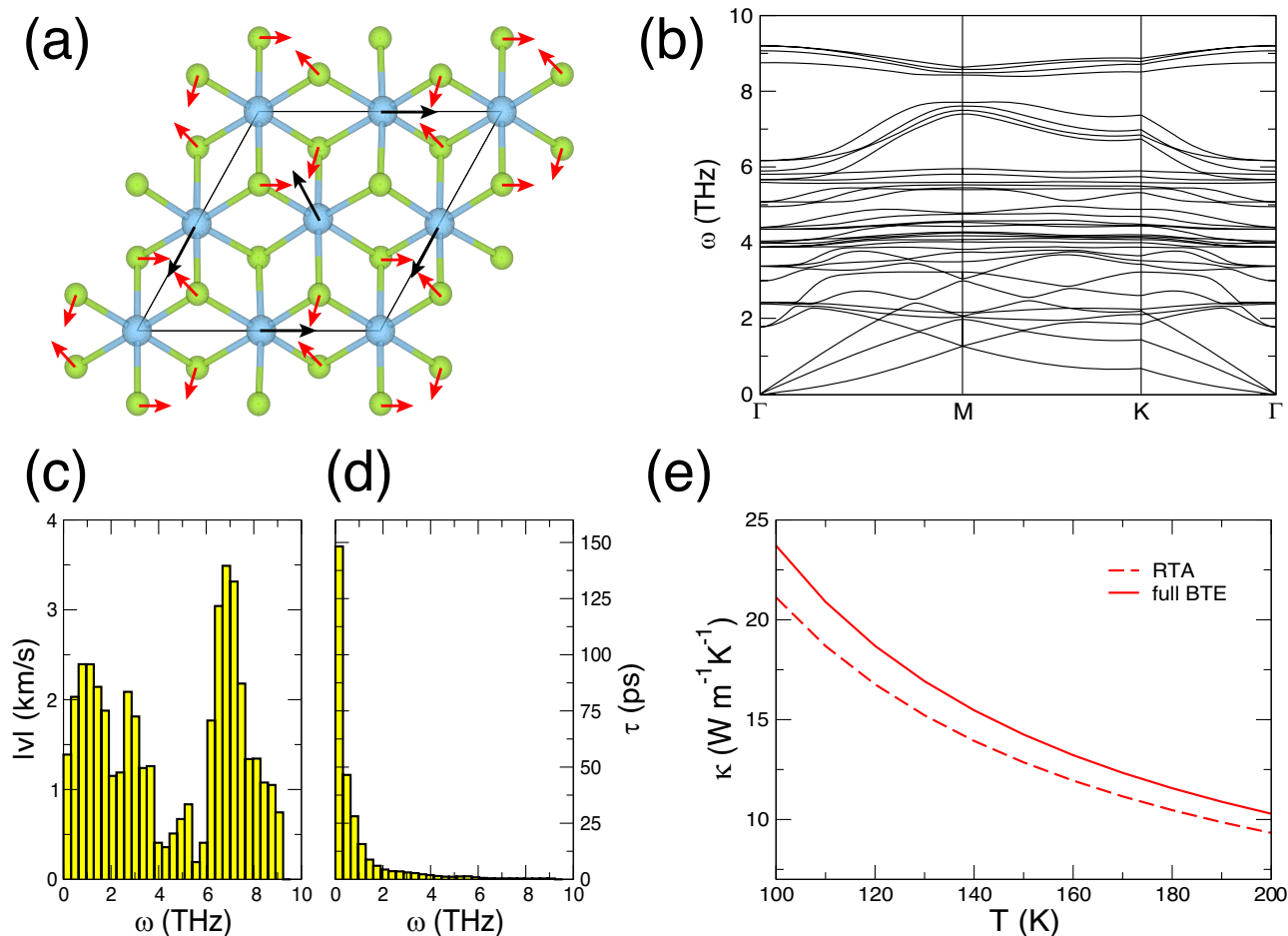


Fig. 2 | Thermal conductivity of the low-temperature CDW ground-state. **a** Structure of the 2×2 CDW. The black and red arrows indicate the distortions, δTi and δSe , respectively (not in scale). **b** Phonon dispersion along the Γ -M-K- Γ path ($\Gamma = 0, 0, 0$; $M = 1/2, 0, 0$; $K = 1/3, 1/3, 0$). **c, d** Phonon velocities and lifetimes as a

function of frequency. **e** Thermal conductivity as a function of temperature as obtained from the iterative solution of the linearized (continuous line) and the RTA (dashed line) phonon BTE.

Electronic thermal conductivity, Seebeck coefficient, and ZT

We used the QUANTUM ESPRESSO (QE) software^{44,45} with similar settings as those used in the lattice thermal conductivity calculations (e.g., PAW, energy cutoffs, the exchange-correlation functional,...), but including a self-consistently calculated Hubbard correction computed using the Hubbard parameters (HP) code⁴⁶, as this shifts the transition range near the experimental value⁴⁷. This last point is of key importance for electronic transport calculations, as it allows to use the same temperature for both the smearing in first-principles calculations and the occupations in the transport calculations. To further illustrate this point, if no Hubbard correction was considered, these two quantities would differ more than 1000 K^{47} .

Harmonic IFCs and the first-derivative of the Kohn-Sham potential with respect to phonon perturbations were obtained using the density perturbation functional theory with Hubbard (DPFT + U), as implemented in the PHONON package included within QUANTUM ESPRESSO suit⁴⁸, using a $12 \times 12 \times 1$ Γ -centered \mathbf{q} -mesh and a strict convergence limit of 1.0^{-16} Ry. Then, the computation of electron-phonon matrix elements and Hamiltonian in the real space was performed with the EPW package⁴⁹, through the wannierization of the isolated manifold composed of 7th–15th band, using SCDM-k method⁵⁰ as implemented in wannier90⁵¹ for the initial projection. We note that the electron-phonon matrix elements do not take into account the Hubbard contribution beyond phonon frequencies and the unperturbed electronic density; nonetheless, the introduction of such effects has been shown to introduce small shifts into the electron-phonon matrix elements⁵².

Following this procedure, the electronic thermal conductivity (κ_{el}), the diffusive Seebeck coefficient (S_{el}), and the electrical conductivity (σ) were obtained by iteratively solving the electronic BTE with `elphbolt`⁵³, until the relative change in all transport coefficients was less than 1.0×10^{-4} .

These quantities together with the lattice conductivity at a given T allow for the computation of the thermoelectric figure of merit:

$$ZT = \frac{\sigma S_{el}^2}{\kappa_{ph} + \kappa_{el}} \tag{6}$$

Notice that, though drag effects were neglected (i.e., the electron and phonon BTEs beyond RTA are solved independently), all ab initio quantities were calculated at that specific electronic temperature, so that we did not merely account for thermal effects on the occupation factors. In this respect, the determination of the electronic temperature for the Gaussian smearing calculation has been performed by matching their phonon frequencies—with a preponderance of the M-point—with the ones computed using a Fermi-Dirac smearing.

Results

Phonon transport in the CDW ground state

Below the critical temperature T_c , which experimentally varies between $\approx 200 \text{ K}^{24}$ and 232 K^{25} , 1L-TiSe₂ exhibits a commensurate CDW 2×2 phase. While in the undistorted high-temperature 1×1 phase there is only one type of octahedra (with six Ti-Se bonds of identical length), in the 2×2

distorted ground state there are two different types of octahedra per unit cell, one of type I and three of type II. Type I octahedra exhibit all six Ti–Se bonds of identical length and are very similar to those found in the undistorted 1×1 phase; type II octahedra, which are those more severely distorted, exhibit two short, two long, and two intermediate Ti–Se bonds, the latter being very similar to those found in type I octahedra. The Ti and Se displacements occur mostly parallel to the layer and, according to an X-ray study⁵⁶, the ratio between the Ti and Se displacements amounts to 3.3 ($\delta\text{Ti} = 0.082 \text{ \AA}$ and $\delta\text{Se} = 0.025 \text{ \AA}$ at $T = 77 \text{ K}$), which is very similar to the value of 3.0 found in bulk TiSe_2 ⁵⁷ (note that in bulk the CDW also leads to doubling of the unit cell along the interlayer direction). The influence of these structural parameters on the electronic properties of 1L- TiSe_2 has been analyzed in detail in a previous work⁵⁸.

Following Calandra and Mauri³⁷, we kept the lattice parameter fixed to the experimental value of 3.5398 \AA and optimized the atomic coordinates. It has been shown³⁸ that this choice yields phonons in excellent agreement with the experiments⁵⁹. We obtained a displacement of the Ti atoms of 0.075 \AA and a corrugation of 0.008 \AA , in agreement with previous results^{39,55,58,60}. The phonon dispersion shown in Fig. 2b is well-behaved and does not present imaginary frequencies, thus corroborating the expected dynamical stability of the distorted 2×2 ground-state phase. Intriguingly, the largest calculated phonon velocities correspond to optical modes, not to acoustic modes, in the frequency range $6 \leq \omega \leq 8 \text{ THz}$ (Fig. 2c). However these optical modes present very strong anharmonic scattering, with lifetimes that are 2–3 orders of magnitude smaller than those of low-frequency phonons ($\omega < 2 \text{ THz}$), and consequently their contribution to κ turns out to be negligible (Fig. 2d).

Our results for the thermal conductivity of the CDW 2×2 phase in the temperature range $100 \leq T \leq 200 \text{ K}$ are shown in Fig. 2e. The CDW becomes unstable at temperatures above 200 K , while below 100 K is difficult to guarantee robust convergence of the computed κ values with respect to the number of \mathbf{q} -points used to solve the BTE, due to the importance of very long wavelength phonons. For the calculation of the thermal conductivity of 2D materials^{61–64}, one usually needs to adopt a particular layer thickness. Here, we assumed it to be equal to 6 \AA , that is, the interlayer separation in bulk TiSe_2 ⁶⁵. Although there are more sophisticated procedures for selecting this parameter (e.g., based on the decay of the electron density away from the atomic planes), here we are mainly concerned with

the variation of κ upon melting of the CDW (i.e., in going from the 2×2 CDW to the 1×1 undistorted phase), hence any reasonable choice of the layer thickness may be expected to provide equivalent results. Under these assumptions, we obtained a κ value of $10 \text{ W m}^{-1} \text{ K}^{-1}$ at 200 K . It is worth noting that the use of the RTA, which is notoriously unreliable for 2D materials where hydrodynamic phonon transport plays an important role^{66–68}, in fact, provides a κ underestimation of approximately 10%. This result stems from the fact that the RTA treats as resistive even those phonon–phonon processes that simply redistribute momentum, and is common to a broad class of 2D materials.

Light-induced CDW melting

At temperatures below T_c , the undistorted 1×1 phase is dynamically unstable. In our zero-temperature calculations, such a vibrational instability manifests as an imaginary phonon mode at the high-symmetry reciprocal point M (Fig. 3). This zone-boundary instability has been widely reported in the literature^{39,58,60,69} and directly hints at the 2×2 periodicity of the CDW phase. Nonetheless, this vibrational instability can be lifted either by electron/hole doping or photoexcitation, which we effectively accounted for by means of the smearing of the Fermi–Dirac distribution that determines the partial occupancies of each orbital, as discussed in the Methods section. In the first case, excess charge is directly injected from the electronic states of extrinsic impurities into the conduction/valence band; in the second case, excitons are photogenerated and electrons are promoted from the valence to the conduction band. Both routes leading to suppression of the CDW instability have been already reported^{58,69–71}. For instance, experimental evidence for photoinduced CDW melting has been provided by M\"ohr-Vorobeva and coworkers²⁶, who also have reported that the CDW $2 \times 2 \rightarrow 1 \times 1$ phase transition takes place during a very short time interval of 250 fs (recovery of the CDW instability upon removal of the light source takes a bit longer, $10 \text{ ps}–100 \text{ ns}$). Figure 3 illustrates both CDW suppression mechanisms as obtained from first-principles calculations. Therein, we plot the phonon dispersion curves obtained for different excess charge carrier densities in the conduction band, n_e . Note that in the photoexcitation case n_e is always compensated by an equal density of excess holes, n_h , in the valence band (in contrast to the extrinsic impurities case, in which only n_e or n_h are present). It is worth mentioning that biaxial strain (or pressure in the case of

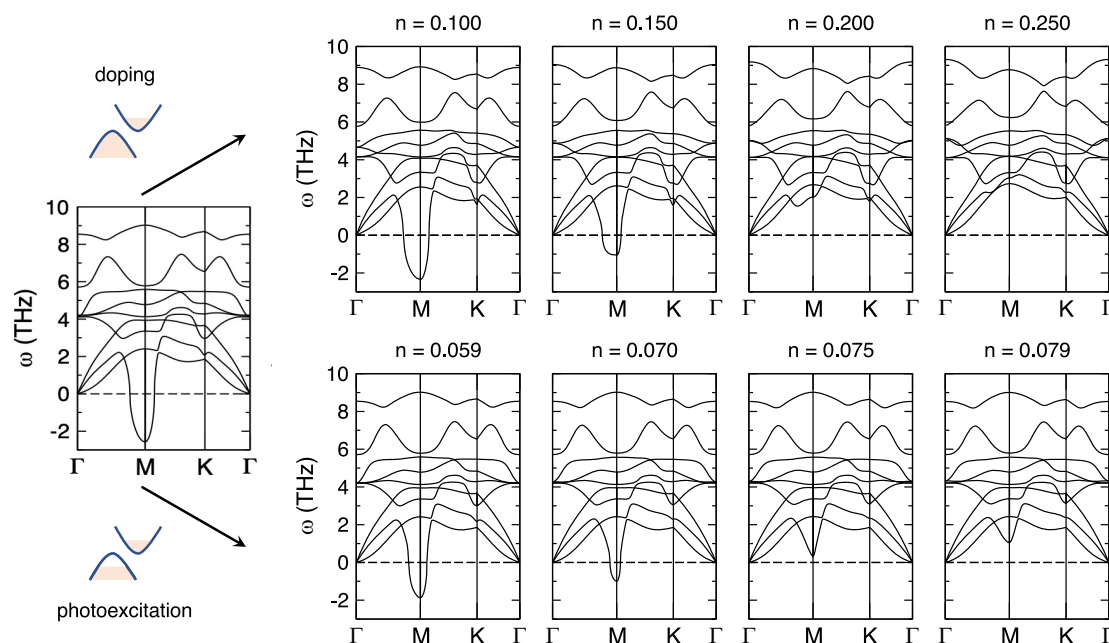


Fig. 3 | Lifting of the dynamical instability of the 1×1 phase. Phonon dispersion of the 1×1 phase for different concentrations, n_e , of charge carriers in the conduction band provided by impurity doping (top row) or photoexcitation (bottom row). The

phonon dispersion of the undoped 1×1 , exhibiting the characteristic instability at the M point, is shown on the left-hand side.

bulk TiSe_2) may also drive the stabilization of the undistorted 1×1 phase at low temperatures, as it has been experimentally^{73,74} and theoretically^{70,75} demonstrated (we will not explicitly address this latter case here).

Two important observations can be made by looking at Fig. 3. First, doping and photoexcitation may provide almost identical phonon dispersion curves although for quite different n_e values (i.e., in the photoexcitation case a lower n_e is needed for CDW melting since, as mentioned above, n_e is always mirrored by an equal density of holes, n_h , which also contributes to the stabilization of the undistorted 1×1 phase⁵⁸). Second, and most importantly for κ tuning, photoexcitation acts almost exclusively on one single phonon mode, the soft mode at the high-symmetry reciprocal point M that drives the CDW instability, leaving the rest of the phonon dispersion essentially unaltered. It is worth noting that, right upon stabilization of the undistorted 1×1 phase this soft phonon mode acquires a “V” shape with an almost linear dispersion around the M point, which is reminiscent of Γ acoustic modes. Indeed, at low charge injections, the soft mode keeps a close resemblance with the unstable mode in *dark* conditions that exhibit a minimum at the M point. As n_e is steadily increased, the frequency of the M phonon mode also increases, eventually merging with the mid-frequency phonon bands.

In order to check the effect of temperature on the phonon dispersion, we have computed finite temperature phonons at 200 K with a normal-mode-decomposition technique⁷⁶, for the 2×2 CDW distorted phase. The comparison with the zero-kelvin phonon dispersion (see Supplementary Fig. 4) suggests that this is a reasonably good approximation. The only noticeable difference is a softening of the highest energy acoustic mode, which deserves further investigation (differences in the optical modes at $\omega > 6$ THz are not playing a role in heat transport; see below the discussion of Fig. 5). Notice also that excitonic effects are not accounted for in our calculations. It has been shown that including them has the main effect of reducing optical transition energies⁷⁷, which we have not addressed in the present manuscript.

Thermal conductivity of the 1×1 phase

Our results for the thermal conductivity of the photo-stabilized 1×1 phase are shown in Fig. 4, where we plot the relative difference, $\Delta\kappa$, with respect to the CDW 2×2 ground state. As it can be appreciated there, for high enough n_e values the thermal conductivity of the 1×1 phase practically matches that of the CDW phase, while for more moderate n_e 's a considerable reduction of up to 25 % is evidenced.

These results in principle may seem counter-intuitive, since, as a general rule, materials with smaller/simpler primitive cells—like that of the 1×1 phase as compared to the CDW ground state—tend to exhibit larger κ values. The reason for this argument is that reduced primitive cells imply smaller numbers of phonon modes hence the occurrence of energy and momentum-conserving phonon–phonon processes, which can reduce κ , is less likely. In the present case, these qualitative arguments, however, only apply to high n_e values for which the main effect of symmetry breaking is to lift a few phonon degeneracies. Figure 5, for instance, shows the phonon dispersion curves obtained along the Γ –M path for the CDW ground state and a strongly doped 1×1 phase; to allow for a direct comparison, the bands of the latter phase were folded, as if they were calculated in a 2×2 supercell. The effects of symmetry breaking are most significant for the optical phonon modes with frequencies 6–7 THz, which split into four branches in the CDW phase. However, phonon modes in that frequency region do not appreciably contribute to κ , as it is shown by the cumulative thermal conductivity plot in the same figure (see also Fig. 2 and related discussion). Differences are also appreciated at lower frequencies, although most of them concern dispersionless optical modes that do not carry heat due to their very low phonon velocities. Heat-carrying acoustic modes, on the other hand, hardly exhibit any difference between the two phases.

By looking at the evolution of phonon dispersion curves in Fig. 3, it is clear that the qualitative explanation given above does not apply to the results obtained for low n_e values. At these conditions, the differences between the phonon bands of the two phases are significant, the 1×1 soft phonon mode with a pronounced minimum around the zone-boundary point M playing a major role. At first glance, however, the $\Delta\kappa$ results obtained in this case also

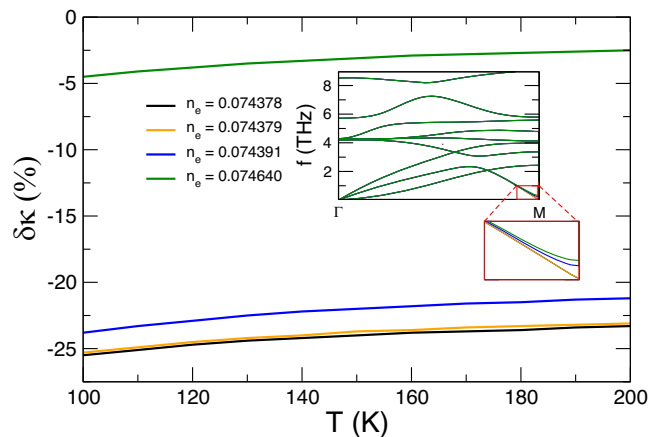


Fig. 4 | Thermal conductivity of the CDW-melted 1×1 phase. Reduction of the thermal conductivity, $\Delta\kappa$, as a function of temperature upon the light-induced melting of the CDW for different concentrations of the photoexcited charge. Inset: phonon dispersion for the values of n_e of the main panel.

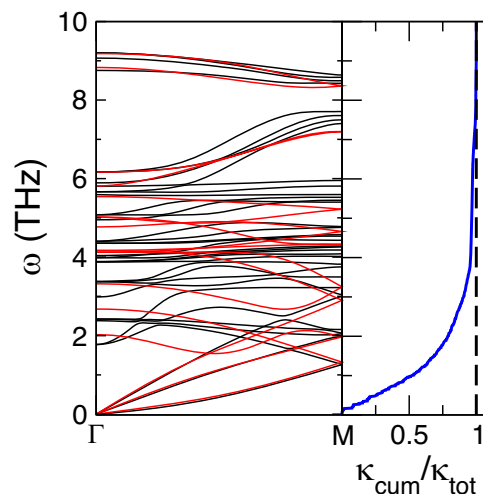


Fig. 5 | High photoexcitation limit. (Left) Comparison between the phonon dispersion of the CDW (black) and the 1×1 phase (red) along the Γ –M path for $n_e = 0.074640$; the latter has been folded to allow a direct comparison. (Right) Cumulative thermal conductivity as a function of phonon frequency of the CDW phase.

seem surprising: the quasilinear dispersion of the 1×1 soft mode around the M point (e.g., case $n_e = 0.075$ in Fig. 3) indicates large phonon velocities, thus suggesting an increase in the thermal conductivity, while the explicitly computed κ values may be ≈ 25 % lower. Nevertheless, we found that phonon–phonon scattering events involving the M soft phonon mode turn out to be especially resistive, as shown in Supplementary Figs. 1 and 2, which account for the resistive character of the collision processes. Moreover, those maps also reveal that the acoustic phonon branches in the 1×1 phase follow the same trend. Thus, the relative κ decrease predicted here for the undistorted phase mainly originated from a surge in the number of resistive phonon–phonon collisions ascribed to the M soft mode and heat-carrying acoustic modes.

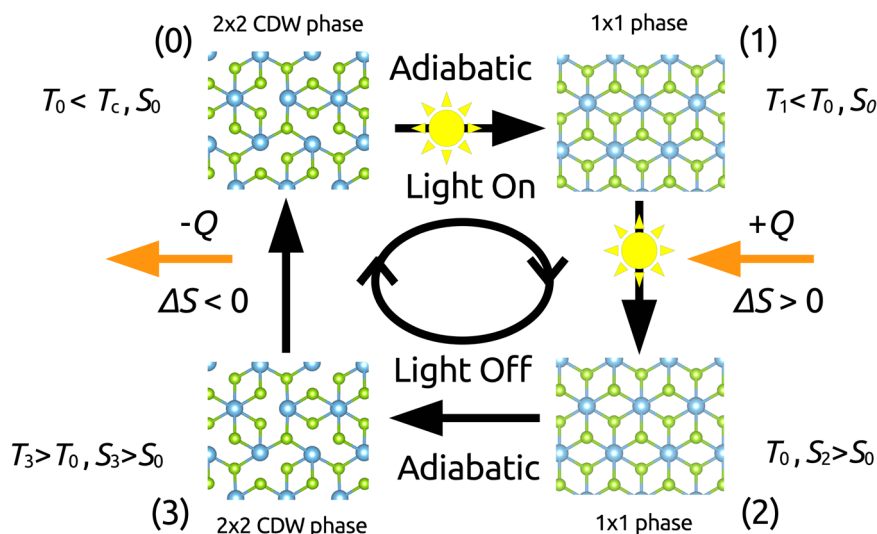
The usual classification of phonon–phonon processes into “Umklapp” and “Normal” has been shown to be not rigorous since it relies on the choice of the primitive cell⁷⁸. Here, nonetheless, it serves as a simple, although qualitative, interpretation of the observed behavior. The low-frequency part of the soft phonon mode lies very close to the Brillouin zone boundary (i.e., the M point) hence practically all the allowed phonon–phonon processes

Table 1 | Thermoelectric properties

T, [K]	κ_{ph} [$\frac{W}{m \cdot K}$]	κ_{el} [$\frac{W}{m \cdot K}$]	σ [$\frac{S}{m}$]	S_{el} [V/K]	ZT
184.984	8.581	4.039×10^{-1}	1.027×10^5	1.232×10^{-4}	3.209×10^{-2}
184.988	8.609	4.077×10^{-1}	1.045×10^5	1.242×10^{-4}	3.307×10^{-2}
185.126	8.809	4.117×10^{-1}	1.050×10^5	1.237×10^{-4}	3.226×10^{-2}
186.876	1.080×10^1	4.321×10^{-1}	1.053×10^5	1.196×10^{-4}	2.507×10^{-2}

Lattice thermal conductivity (κ_{ph}), electronic thermal conductivity (κ_{el}), diffusive Seebeck coefficient (S_{el}), electrical conductivity (σ), and thermoelectric figure of merit (ZT) for 1×1 1L-TiSe₂ for four different temperatures (T).

Fig. 6 | Photocaloric cycle. Sketch of the four-step refrigeration cycle based on the photocaloric effect.



involving it will have a quasimomentum lying outside the first Brillouin zone, which is the signature of Umklapp processes. These processes destroy phonon momentum and are purely resistive, in accordance with the values shown in Supplementary Fig. 2.

As a final remark, it is important to stress that the κ differences between the CDW 2×2 and undistorted 1×1 phases can be almost entirely traced back to one single phonon mode. The rest of the phonon dispersion curves hardly undergo any change under varying n_e . This can be clearly appreciated in the inset of Fig. 4, where the undistorted 1×1 phonon bands corresponding to thermal conductivities represented in the same figure as a function of n_e appear virtually indistinguishable. A zoomed-in view of the phonon branches at wave vectors around the M point is necessary to reveal definite differences.

Electronic thermal conductivity

The absence vs occurrence of a small bandgap for undistorted 1×1 1L-TiSe₂ is unclear, due to the difficulty in preparing non-doped samples. However, experimental results clearly show a drastic reconstruction of the electronic structure and a semiconducting character when the 2×2 CDW occurs⁵⁴. These considerations can be important for the κ tuning discussed because a metallic 1×1 phase would also feature a non-negligible contribution to the total thermal conductivity, which could partially compensate for the effect reported above (the 1×1 phase has a lower phononic conductivity than the CDW phase).

In view of this possibility, we explicitly calculated the electronic contribution to the thermal conductivity for the undistorted 1×1 phase, κ_{el} , along with some related quantities like the diffusive Seebeck coefficient, S_{el} , and electrical conductivity, σ . We find it worth mentioning that, due to the limitations of LDA in providing accurate band structure for highly correlated systems and the sensitivity of the electronic properties to this, we employed LDA + U to better match experimental results. The on-site

Coulomb interaction (U) was determined self-consistently for different smearing values, something crucial for an accurate description of the CDW transition^{39,47}. According to the results shown in Table 1, thermal transport in the 1×1 phase is almost entirely governed by the atomic lattice since the electronic thermal conductivity can be neglected to all practical effects. Consequently, the large photoinduced κ changes driven by the melting of the CDW are predominantly of phononic nature. Furthermore, the results in Table 1 also show that although the 1×1 phase cannot be regarded as a superb thermoelectric material (i.e., the corresponding thermoelectric figures of merit, ZT, approximately amount to 0.03) is still comparable in performance to some other well-known semiconductors (e.g., doped Si, which as a reference displays a ZT in the range of 0.004–0.011 at around 200 K⁷⁹), thus offering room for further improvements.

Envisaged applications: solid-state cooling

Besides the realization of *phononic devices*^{1–3}, the photoinduced 2×2 CDW \rightarrow 1×1 phase transition in 1L-TiSe₂ also holds great promise for developing solid-state cooling applications based on thermoelectricity^{80,81} (see above) and novel caloric effects^{82,83}, as we explain next.

Under external field (e.g., pressure and electric bias) variations, caloric materials experience large adiabatic temperature variations ($|\Delta T| \sim 1–10$ K) as a result of phase transformations entailing large isothermal entropy changes ($|\Delta S| \sim 10–100$ J K⁻¹ kg⁻¹). Such caloric effects may be exploited for engineering solid-state refrigeration cycles^{82,83}. The large photoinduced lattice κ variation unraveled here for TiSe₂ hints also at the existence of large isothermal entropy changes driven by light absorption (i.e., photocaloric effects). In fact, our first-principles calculations render sizeable $|\Delta S|$ values of ≈ 6 J K⁻¹ kg⁻¹ for photoexcited charge densities of around $0.074 e \text{ \AA}^{-3}$ at $T = 200$ K, 2×2 CDW being the phase presenting the lowest entropy.

A possible four-step refrigeration cycle based on the photocaloric effect disclosed here for TiSe₂ may be envisaged (see Fig. 6). First, starting from the

low-entropy 2×2 CDW phase at $T_0 < T_c$, the system will be adiabatically irradiated with light until stabilizing the high-entropy 1×1 phase. As a consequence, the temperature of the TiSe_2 sample will decrease, $T_1 < T_0$ (i.e., inverse photocaloric effect, $\Delta T < 0$). Second, by keeping the light conditions on, the sample will be put into contact with the targeted body to be refrigerated so that heat, $|Q| = T|\Delta S|$, will be transferred to TiSe_2 until restoring the initial temperature conditions, $T_2 = T_0$. Third, the light irradiation will be adiabatically removed thus stabilizing again the low-entropy 2×2 CDW phase. Consequently, the temperature of the TiSe_2 sample will increase, $T_3 > T_0$. Fourth, the sample will be put into contact with a heat sink so that heat will be removed from TiSe_2 until restoring the initial temperature conditions, $T_4 = T_0$, thus completing a cooling cycle. An approximate estimation of the efficiency of the four-step refrigeration cycle just described, which considers $|Q|$, the amount of heat associated with the photocaloric effect, and the minimum electronic work that is necessary to trigger the CDW melting in TiSe_2 , amounts to 34%.

Such a possible solid-state cooling cycle presents a clear drawback: the operation conditions for TiSe_2 should be $T_0 < 200$ K, which is well below room temperature. (This practical limitation, however, may be overcome by finding analogous CDW materials presenting higher critical temperatures.) On the other hand, the described refrigeration cycle is very promising in several aspects, namely, (1) the temperature span over which it could be operated is unusually ample (~ 100 K) since the underlying photoinduced phase transition is not restricted from below T_c , (2) due to the two-dimensional nature of TiSe_2 , light absorption may be achieved very efficiently, and (3) the proposed refrigeration cycle is well suited for miniaturization. Noteworthy, an analogous cycle with a giant room-temperature photocaloric effect has been recently reported in a ferroelectric perovskite⁸⁴.

Discussion

We have reported first-principles calculations hinting at a dynamical and reversible modulation of the thermal conductivity of 1L- TiSe_2 driven by photoinduced melting of its CDW. Such changes occur in an ultrafast timescale of picoseconds and can be also obtained by field-controlled activation of impurity doping. The lower thermal conductivity of the undistorted 1×1 phase stems from the resistive character of phonon-phonon processes involving a high-symmetry soft mode, which otherwise is responsible for the stabilization of the distorted CDW 2×2 phase. These findings should be general to few-layer and bulk TiSe_2 , featuring an analogous lattice distortion below a similar critical temperature, and to other CDW materials³⁰, and thus open new avenues in the design of thermal devices in which information is encoded through phonons and that require of materials with fast and dynamical thermal responsiveness. The existence of sizeable photocaloric effects in 1L- TiSe_2 is also proposed, which may find applications in solid-state nanocooling.

Data availability

The data that support the findings of this study are available from the authors upon reasonable request. The files of the calculations of the thermal conductivity are freely available at <https://doi.org/10.20350/digitalCSIC/15718>.

Received: 10 June 2024; Accepted: 19 September 2024;

Published online: 30 September 2024

References

- Li, N. et al. *Colloquium: phononics: manipulating heat flow with electronic analogs and beyond*. *Rev. Mod. Phys.* **84**, 1045 (2012).
- Volz, S. et al. Nanophononics: state of the art and perspectives. *Eur. Phys. J. B* **89**, 15 (2016).
- Swoboda, T., Klinar, K., Yalamarthi, A. S., Kitanovski, A. & Muñoz Rojo, M. Thermal control devices: solid-state thermal control devices. *Adv. Elec. Mater.* **7**, 2170008 (2021).
- Moore, A. L. & Shi, L. Emerging challenges and materials for thermal management of electronics. *Mater. Today* **17**, 163 (2014).
- Zeng, Y. et al. Extreme fast charging of commercial Li-ion batteries via combined thermal switching and self-heating approaches. *Nat. Commun.* **14**, 3229 (2023).
- Wehmeyer, G., Yabuki, T., Monachon, C., Wu, J. & Dames, C. Thermal diodes, regulators, and switches: physical mechanisms and potential applications. *Appl. Phys. Rev.* **4**, 041304 (2017).
- Ihlefeld, J. F. et al. Room-temperature voltage tunable phonon thermal conductivity via reconfigurable interfaces in ferroelectric thin films. *Nano Lett.* **15**, 1791 (2015).
- Langenberg, E. et al. Ferroelectric domain walls in PbTiO_3 are effective regulators of heat flow at room temperature. *Nano Lett.* **19**, 7901 (2019).
- Aryana, K. et al. Observation of solid-state bidirectional thermal conductivity switching in antiferroelectric lead zirconate (PbZrO_3). *Nat. Commun.* **13**, 1573 (2022).
- Negi, A. et al. Ferroelectric domain wall engineering enables thermal modulation in PMN-PT single crystals. *Adv. Mater.* **35**, 2211286 (2023).
- Wang, J.-J., Wang, Y., Ihlefeld, J. F., Hopkins, P. E. & Chen, L.-Q. Tunable thermal conductivity via domain structure engineering in ferroelectric thin films: a phase-field simulation. *Acta Mater.* **111**, 220 (2016).
- Seijas-Bellido, J. A. et al. A phononic switch based on ferroelectric domain walls. *Phys. Rev. B* **96**, 140101(R) (2017).
- Royo, M., Escorihuela-Salayero, C., Íñiguez, J. & Rurali, R. Ferroelectric domain wall phonon polarizer. *Phys. Rev. Mater.* **1**, 051402(R) (2017).
- Liu, C., Chen, Y. & Dames, C. Electric-field-controlled thermal switch in ferroelectric materials using first-principles calculations and domain-wall engineering. *Phys. Rev. Appl.* **11**, 044002 (2019).
- Dangić, Đ., Murray, É. D., Fahy, S. & Savić, I. Structural and thermal transport properties of ferroelectric domain walls in GeTe from first principles. *Phys. Rev. B* **101**, 184110 (2020).
- Qin, G., Qin, Z., Yue, S.-Y., Yan, Q.-B. & Hu, M. External electric field driving the ultra-low thermal conductivity of silicene. *Nanoscale* **9**, 7227 (2017).
- Seijas-Bellido, J. A., Aramberri, H., Íñiguez, J. & Rurali, R. Electric control of the heat flux through electrophononic effects. *Phys. Rev. B* **97**, 184306 (2018).
- Seijas-Bellido, J. A., Íñiguez, J. & Rurali, R. Anisotropy-driven thermal conductivity switching and thermal hysteresis in a ferroelectric. *Appl. Phys. Lett.* **115**, 192903 (2019).
- Torres, P., Seijas-Bellido, J. A., Escorihuela-Salayero, C., Íñiguez, J. & Rurali, R. Theoretical investigation of lattice thermal conductivity and electrophononic effects in SrTiO_3 . *Phys. Rev. Mater.* **3**, 044404 (2019).
- Torres, P., Íñiguez, J. & Rurali, R. Giant electrophononic response in PbTiO_3 by strain engineering. *Phys. Rev. Lett.* **123**, 185901 (2019).
- Yang, Z., Yuan, K., Meng, J. & Hu, M. Electric field tuned anisotropic to isotropic thermal transport transition in monolayer borophene without altering its atomic structure. *Nanoscale* **12**, 19178 (2020).
- Cazorla, C. & Rurali, R. Dynamical tuning of the thermal conductivity via magnetophononic effects. *Phys. Rev. B* **105**, 104401 (2022).
- Cazorla, C., Stengel, M., Íñiguez, J. & Rurali, R. Giant multiphononic effects in a perovskite oxide. *npj Comput. Mater.* **9**, 97 (2023).
- Morosan, E. et al. Superconductivity in Cu_xTiSe_2 . *Nat. Phys.* **2**, 544 (2006).
- Watson, M. D. et al. Strong-coupling charge density wave in monolayer TiSe_2 . *2D Mater.* **8**, 015004 (2021).
- Möhr-Vorobeva, E. et al. Nonthermal melting of a charge density wave in TiSe_2 . *Phys. Rev. Lett.* **107**, 036403 (2011).
- Burian, M. et al. Structural involvement in the melting of the charge density wave in 1T- TiSe_2 . *Phys. Rev. Res.* **3**, 013128 (2021).

28. Huber, M. et al. Ultrafast creation of a light-induced semimetallic state in strongly excited 1T-TiSe₂. *Sci. Adv.* **10**, ead14481 (2024).
29. Li, B., Wang, L. & Casati, G. Negative differential thermal resistance and thermal transistor. *Appl. Phys. Lett.* **88**, 143501 (2006).
30. Pouget, J.-P. & Canadell, E. Structural approach to charge density waves in low-dimensional systems: electronic instability and chemical bonding. *Rep. Prog. Phys.* **87**, 026501 (2024).
31. Kresse, G. & Furthmüller, J. Efficient iterative schemes for ab initio total-energy calculations using a plane-wave basis set. *Phys. Rev. B* **54**, 11169 (1996).
32. Kresse, G. & Furthmüller, J. Efficiency of ab-initio total energy calculations for metals and semiconductors using a plane-wave basis set. *Comp. Mater. Sci.* **6**, 15 (1996).
33. Blöchl, P. E. Projector augmented-wave method. *Phys. Rev. B* **50**, 17953 (1994).
34. Kresse, G. & Joubert, D. From ultrasoft pseudopotentials to the projector augmented-wave method. *Phys. Rev. B* **59**, 1758 (1999).
35. Perdew, J. P. & Zunger, A. Self-interaction correction to density-functional approximations for many-electron systems. *Phys. Rev. B* **23**, 5048 (1981).
36. Ceperley, D. M. & Alder, B. J. Ground state of the electron gas by a stochastic method. *Phys. Rev. Lett.* **45**, 566 (1980).
37. Calandra, M. & Mauri, F. Charge-density wave and superconducting dome in TiSe₂ from electron–phonon interaction. *Phys. Rev. Lett.* **106**, 196406 (2011).
38. Calandra, M. & Mauri, F. Calandra and Mauri reply. *Phys. Rev. Lett.* **112**, 049702 (2014).
39. Bianco, R., Calandra, M. & Mauri, F. Electronic and vibrational properties of TiSe₂ in the charge-density-wave phase from first principles. *Phys. Rev. B* **92**, 094107 (2015).
40. Togo, A. & Tanaka, I. First principles phonon calculations in materials science. *Scr. Mater.* **108**, 1 (2015).
41. Li, W., Carrete, J., Katcho, N. A. & Mingo, N. ShengBTE: a solver of the Boltzmann transport equation for phonons. *Comp. Phys. Commun.* **185**, 1747 (2014).
42. Raya-Moreno, M., Carroixà, X. & Carrete, J. BTE-Barna: an extension of almaBTE for thermal simulation of devices based on 2D materials. *Comput. Phys. Commun.* **281**, 108504 (2022).
43. Dongre, B. et al. Combined treatment of phonon scattering by electrons and point defects explains the thermal conductivity reduction in highly-doped Si. *J. Mater. Chem. A* **8**, 1273 (2020).
44. Giannozzi, P. et al. QUANTUM ESPRESSO: a modular and open-source software project for quantum simulations of materials. *J. Phys. Condens. Matter* **21**, 395502 (2009).
45. Giannozzi, P. et al. Advanced capabilities for materials modelling with QUANTUM ESPRESSO. *J. Phys. Condens. Matter* **29**, 465901 (2017).
46. Timrov, I., Marzari, N. & Cococcioni, M. HP—a code for the calculation of Hubbard parameters using density-functional perturbation theory. *Comput. Phys. Commun.* **279**, 108455 (2022).
47. Novko, D., Torbatian, Z. & Lončarić, I. Electron correlations rule the phonon-driven instability in single-layer TiSe₂. *Phys. Rev. B* **106**, 245108 (2022).
48. Floris, A. et al. Hubbard-corrected density functional perturbation theory with ultrasoft pseudopotentials. *Phys. Rev. B* **101**, 064305 (2020).
49. Poncé, S., Margine, E., Verdi, C. & Giustino, F. EPW: electron–phonon coupling, transport and superconducting properties using maximally localized Wannier functions. *Comput. Phys. Commun.* **209**, 116 (2016).
50. Damle, A., Lin, L. & Ying, L. SCDM-k: localized orbitals for solids via selected columns of the density matrix. *J. Comput. Phys.* **334**, 1 (2017).
51. Mostofi, A. A. et al. An updated version of wannier90: a tool for obtaining maximally-localised Wannier functions. *Comput. Phys. Commun.* **185**, 2309 (2014).
52. Zhou, J.-J. et al. Ab initio electron–phonon interactions in correlated electron systems. *Phys. Rev. Lett.* **127**, 126404 (2021).
53. Protik, N. H., Li, C., Pruneda, M., Broido, D. & Ordejón, P. The elphbolt ab initio solver for the coupled electron–phonon Boltzmann transport equations. *npj Comput. Mater.* **8**, 28 (2022).
54. Sugawara, K. et al. Unconventional charge-density-wave transition in monolayer 1T-TiSe₂. *ACS Nano* **10**, 1341 (2016).
55. Chen, P. et al. Charge density wave transition in single-layer titanium diselenide. *Nat. Commun.* **6**, 8943 (2015).
56. Fang, X.-Y., Hong, H., Chen, P. & Chiang, T.-C. X-ray study of the charge-density-wave transition in single-layer TiSe₂. *Phys. Rev. B* **95**, 201409(R) (2017).
57. Di Salvo, F. J., Moncton, D. E. & Waszczak, J. V. Electronic properties and superlattice formation in the semimetal TiSe₂. *Phys. Rev. B* **14**, 4321 (1976).
58. Guster, B., Canadell, E., Pruneda, M. & Ordejón, P. First principles analysis of the CDW instability of single-layer 1T-TiSe₂ and its evolution with charge carrier density. *2D Mater.* **5**, 025024 (2018).
59. Weber, F. et al. Electron–phonon coupling and the soft phonon mode in TiSe₂. *Phys. Rev. Lett.* **107**, 266401 (2011).
60. Singh, B., Hsu, C.-H., Tsai, W.-F., Pereira, V. M. & Lin, H. Stable charge density wave phase in a 1T-TiSe₂ monolayer. *Phys. Rev. B* **95**, 245136 (2017).
61. Gu, X., Wei, Y., Yin, X., Li, B. & Yang, R. Colloquium: phononic thermal properties of two-dimensional materials. *Rev. Mod. Phys.* **90**, 041002 (2018).
62. Ren, W. et al. Impact of moiré superlattice on atomic stress and thermal transport in van der Waals heterostructures. *Appl. Phys. Rev.* **10**, 041404 (2023).
63. Jiang, J.-H., Lu, S. & Chen, J. Phonon focusing effect in an atomic level triangular structure. *Chin. Phys. Lett.* **40**, 096301 (2023).
64. Lu, S., Zhang, Z., Li, Y., Hänggi, P. & Chen, J. Phononic metagrating for lattice wave manipulation. *Phys. Rev. B* **109**, 075404 (2024).
65. Riekel, C. Structure refinement of TiSe₂ by neutron diffraction. *J. Solid. State Chem.* **17**, 389 (1976).
66. Cepellotti, A. et al. Phonon hydrodynamics in two-dimensional materials. *Nat. Commun.* **6**, 6400 (2020).
67. Lindsay, L., Katre, A., Cepellotti, A. & Mingo, N. Perspective on ab initio phonon thermal transport. *J. Appl. Phys.* **126**, 050902 (2019).
68. Jiang, J., Lu, S., Ouyang, Y. & Chen, J. How hydrodynamic phonon transport determines the convergence of thermal conductivity in two-dimensional materials. *Nanomaterials* **12**, 2854 (2022).
69. Zhou, J. S. et al. Anharmonicity and doping melt the charge density wave in single-layer TiSe₂. *Nano Lett.* **20**, 4809 (2020).
70. Wei, M. J. et al. Manipulating charge density wave order in monolayer 1T-TiSe₂ by strain and charge doping: a first-principles investigation. *Phys. Rev. B* **96**, 165404 (2017).
71. Fu, Z.-G. et al. Doping stability and charge-density-wave transition of strained 1T-TiSe₂ monolayer. *EPL* **120**, 17006 (2017).
72. Kusmartseva, A. F., Sipos, B., Berger, H., Forró, L. & Tutiš, E. Pressure induced superconductivity in pristine 1T-TiSe₂. *Phys. Rev. Lett.* **103**, 236401 (2009).
73. Snow, C. S., Karpus, J. F., Cooper, S. L., Kidd, T. E. & Chiang, T.-C. Quantum melting of the charge–density–wave state in 1T-TiSe₂. *Phys. Rev. Lett.* **91**, 136402 (2003).
74. Moulding, O., Muramatsu, T., Sayers, C. J., Como, E. D. & Friedemann, S. Suppression of charge–density–wave order in TiSe₂ studied with high-pressure magnetoresistance. *Electron. Struct.* **4**, 035001 (2022).
75. Olevano, V., Cazzaniga, M., Ferri, M., Caramella, L. & Onida, G. Comment on “charge–density wave and superconducting dome in TiSe₂ from electron–phonon interaction”. *Phys. Rev. Lett.* **112**, 049701 (2014).
76. Carreras, A., Togo, A. & Tanaka, I. DynaPhoPy: a code for extracting phonon quasiparticles from molecular dynamics simulations. *Comput. Phys. Commun.* **221**, 221 (2017).

77. Peng, B. et al. Sub-picosecond photo-induced displacive phase transition in two-dimensional MoTe₂. *npj 2D Mater. Appl.* **4**, 14 (2020).
78. Maznev, A. A. & Wright, O. B. Demystifying umklapp vs normal scattering in lattice thermal conductivity. *Am. J. Phys.* **82**, 1062 (2014).
79. Weber, L. & Gmelin, E. Transport properties of silicon. *Appl. Phys. A* **53**, 136 (1991).
80. Mao, J., Chen, G. & Ren, Z. Thermoelectric cooling materials. *Nat. Mater.* **20**, 454 (2021).
81. Ziabari, A., Zebajadi, M., Vashaei, D. & Shakouri, A. Nanoscale solid-state cooling: a review. *Rep. Prog. Phys.* **79**, 095901 (2016).
82. Hou, H., Qian, S. & Takeuchi, I. Materials, physics and systems for multicaloric cooling. *Nat. Rev. Mater.* **94**, 633 (2022).
83. Cazorla, C. Novel mechanocaloric materials for solid-state cooling applications. *Appl. Phys. Rev.* **6**, 041316 (2019).
84. Rurali, R., Escorihuela-Sayalero, C., Tamarit, J. L., Íñiguez González, J. & Cazorla, C. Giant photocaloric effects across a vast temperature range in ferroelectric perovskites. *Phys. Rev. Lett.* **133**, 11601 (2024).

Acknowledgements

R.R. thanks Maurizia Palummo for the useful discussions. We acknowledge financial support by MCIN/AEI/10.13039/501100011033 under grants PID2020-119777GB-I00 and PID2022-139776NB-C61, the “Ramón y Cajal” fellowship RYC2018-024947-I and the Severo Ochoa Centres of Excellence Program (CEX2019-000917-S), and by the Generalitat de Catalunya under grant no. and 2021 SGR 01519. Calculations were performed at the Centro de Supercomputación de Galicia (CESGA) within action FI-2022-1-0012 of the Red Española de Supercomputación (RES).

Author contributions

R.R. conceived the project. M.R.-M carried out the DFT and the heat transport calculations. E.C. and C.C. provided critical input about the CDW instability and the caloric effect and supervised those calculations. All authors contributed to discussions and the final manuscript.

Competing interests

The authors declare no competing interests.

Additional information

Supplementary information The online version contains supplementary material available at <https://doi.org/10.1038/s41699-024-00501-9>.

Correspondence and requests for materials should be addressed to Riccardo Rurali.

Reprints and permissions information is available at <http://www.nature.com/reprints>

Publisher's note Springer Nature remains neutral with regard to jurisdictional claims in published maps and institutional affiliations.

Open Access This article is licensed under a Creative Commons Attribution-NonCommercial-NoDerivatives 4.0 International License, which permits any non-commercial use, sharing, distribution and reproduction in any medium or format, as long as you give appropriate credit to the original author(s) and the source, provide a link to the Creative Commons licence, and indicate if you modified the licensed material. You do not have permission under this licence to share adapted material derived from this article or parts of it. The images or other third party material in this article are included in the article's Creative Commons licence, unless indicated otherwise in a credit line to the material. If material is not included in the article's Creative Commons licence and your intended use is not permitted by statutory regulation or exceeds the permitted use, you will need to obtain permission directly from the copyright holder. To view a copy of this licence, visit <http://creativecommons.org/licenses/by-nc-nd/4.0/>.

© The Author(s) 2024